PLANT SCIENCES

Conformational cycle and small-molecule inhibition mechanism of a plant ABCB transporter in lipid membranes

Yong Liu[1] and Maofu Liao[1,2]*

In plants, ATP-binding cassette (ABC) transporters are crucial for nutrient uptake, phytohormone transport, and environmental response. It is of great interest to understand the mechanisms of these transporters and develop small-molecule modulators to regulate plant growth. *Arabidopsis* ABCB19 was recently shown to transport brassinosteroid, shaping hormone dynamics and plant architecture. However, the conformational cycle and inhibitor mechanism of ABCB transporters remain elusive. We reconstituted ABCB19 into lipid nanodiscs, where activity was drastically higher than in detergents, and determined its cryo–electron microscopy structures in substrate-free, substrate-bound, vanadate-trapped, and inhibitor-bound states. Inward-facing ABCB19 moved inward upon substrate binding and fully closed with vanadate trapping, unexpectedly temperature dependent. Two inhibitor molecules locked ABCB19 in the inward-facing conformation. Mutagenesis identified key residues for substrate and inhibitor binding, revealing differential contributions to transporter function and inhibition. These results deepen knowledge of plant ABCB transporters, laying a foundation for targeted manipulation to enhance plant resilience and productivity.

INTRODUCTION

ATP-binding cassette (ABC) transporters are a large and diverse family of integral membrane proteins present in all domains of life. These transporters use the energy from ATP binding and hydrolysis to transport a wide range of substrates across cellular membranes (*1*) and play critical roles in various physiological processes including nutrient uptake, toxin efflux, and signal transduction, thus being essential for cellular homeostasis and organismal survival (*2*–*5*). In plants, ABC transporters play a crucial role in regulating nutrient uptake and facilitating the transport of phytohormones, such as auxin, abscisic acid, gibberellins, and cytokinins, thus critically regulating plant growth, development, and stress adaptation (*6*), and transport secondary metabolites that enhance plant defenses against herbivores and pathogens (*7*). Thus, ABC transporters in plants are integral to maintaining homeostasis and enabling adaptation to ever-changing conditions, underscoring their potential as targets for enhancing plant resilience and productivity (*8*).

Substantial advances have been made in understanding plant ABC transporter mechanisms. Techniques like cryo–electron microscopy (cryo-EM) have revealed high-resolution structures of these transporters, providing insights into their architecture and function. Structural analyses have uncovered conformational changes associated with ATP binding and hydrolysis, illustrating how energy from ATP binding and hydrolysis is coupled to substrate movement (*9*). This has led to the identification of specific binding sites for various substrates, highlighting the structural basis for substrate specificity and regulation. For instance, structures of ABCB and ABCG members have elucidated how these proteins interact with different hormone substrates such as brassinosteroid (BR) (*10*–*12*), jasmonic acid (*13*), and abscisic acid (*14*–*16*). Progress has also been made in developing small-molecule inhibitors targeting plant ABC transporters. These inhibitors are valuable for understanding the roles of specific transporters and modulating their activity to enhance plant traits. For example, inhibitors targeting ABCB19 affect plant development and offer tools for regulating plant architecture (*17*).

ABCB transporters were first identified as auxin transporters in 2005 (*18*), and over the subsequent two decades, ABCB1 and ABCB19 have been extensively studied as key auxin efflux transporters contributing to auxin gradient formation, essential for organogenesis, tropisms, and vascular patterning (*19*–*22*). Recent findings indicate that ABCB1 and ABCB19 also play crucial roles in transporting BRs, demonstrating their versatility in modulating hormone dynamics (*10*, *11*). However, the conformational changes associated with substrate transport and the ATPase cycle in ABCB19 remain unclear, and the molecular mechanisms underlying specific inhibitors are yet to be elucidated.

In this study, we performed functional and cryo-EM studies of nanodisc-embedded ABCB19 and determined the structures of ABCB19 in substrate-free, substrate-bound, inhibitor-bound, and vanadate-trapped states. Our results have delineated the conformational cycle of ABCB19 and revealed the structural basis of small-molecule inhibitor, thus advancing our understanding of the function and inhibition of plant ABCB transporters.

RESULTS

ABCB19 in lipid membranes displayed drastically increased activity

Numerous studies demonstrate the importance of membrane environment to support the activity, structure and dynamics of ABC transporters (*23*–*26*). A recent study of ABCB19 in detergents shows low basal ATPase activity (29.6 nmol ATP/min per milligram of protein or 4.0 mol ATP/min per mole of protein) and moderate brassinolide (BL) stimulation (V_{max} = 133.5 nmol ATP/min per milligram of protein or 18.3 mol ATP/min per mole of protein) (*11*). To better

[1]Department of Chemical Biology, School of Life Sciences, Southern University of Science and Technology, Shenzhen, China. [2]Institute for Biological Electron Microscopy, Southern University of Science and Technology, Shenzhen, China.
*Corresponding author. Email: liaomf@sustech.edu.cn

understand the function and structure of ABCB19 in a lipid environment, we set out to purify ABCB19 and reconstitute it into nanodiscs. ABCB19 fused with green fluorescent protein (GFP) and Strep tags at the C terminus was expressed in human embryonic kidney (HEK) 293F cells. The cofactor twisted dwarf 1 (TWD1), essential for folding and membrane targeting of ABCB19, was coexpressed to boost the yield of correctly folded protein (fig. S1A) (*27*, *28*). Following expression, ABCB19 was extracted from the cell membrane using a mixture of 1% *n*-dodecyl-β-D-maltoside (DDM) and 0.2% cholesteryl hemisuccinate (CHS) and subsequently reconstituted into nanodiscs (fig. S1, B to E).

Our ABCB19 preparation in DDM-CHS showed an ATPase activity of 4.1 mol ATP/min per mole of protein, which is similar to a recent report (*11*). The activity of ABCB19 in nanodiscs (87 mol ATP/min per mole of protein) was more than 20 times higher (Fig. 1A), indicating the critical role of lipid membrane in supporting ABCB19 function. The robust activity of nanodisc-embedded ABCB19 is ATP concentration dependent, exhibiting a maximum ATP hydrolysis velocity (V_{max}) of 140.1 mol ATP/min per mole of protein and an apparent K_m of 1.08 mM (fig. S1F). Addition of BL further increased the activity of ABCB19 by threefold (Fig. 1A). In the presence of 2 μM BL, ABCB19 exhibited a V_{max} of 339.9 mol ATP/min per mole of protein and an apparent K_m of 0.24 mM (fig. S1F), demonstrating a clear stimulation of both ATP binding and hydrolysis. In the presence of 2 to 8 μM BL, ABCB19 in nanodiscs reached the highest activity, which is 50 times higher than the activity of ABCB19 in detergents, but a further increase in BL concentration led to marked inhibition (Fig. 1B). Such concentration-dependent dual effects of BL align with in vivo study showing that BRs have dual roles in plant growth: Low concentrations promote root growth and symbiosis by enhancing cell elongation and meristem activity, whereas high concentrations inhibit these processes, reducing root growth (*29*). Our observations are also reminiscent of the homologous human multidrug ABC transporter ABCB1 (Pgp) whose ATPase activity is stimulated and inhibited with low and high drug concentrations, respectively (*30*).

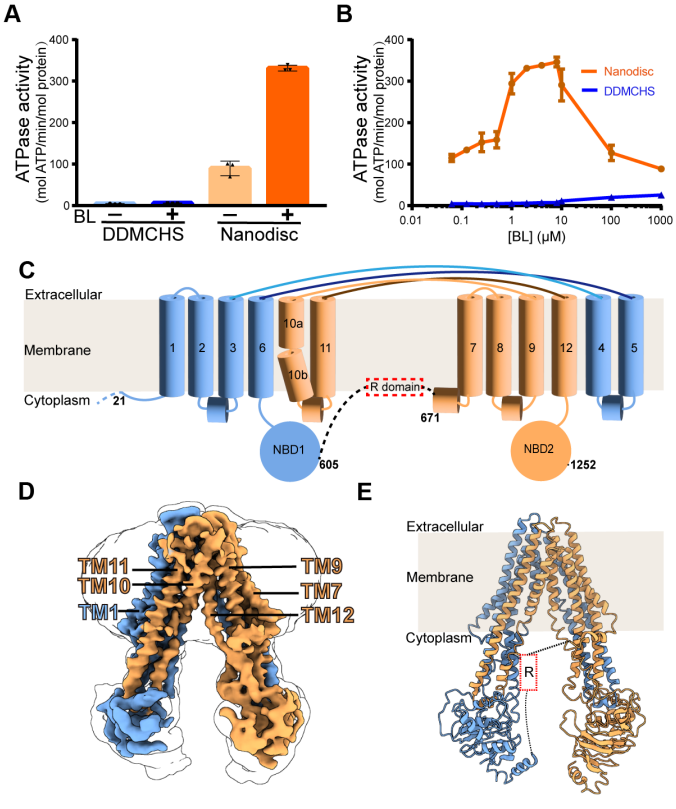

Fig. 1. ATPase activity and structure of ABCB19 in nanodiscs. (**A**) ATPase activities of ABCB19 in DDM-CHS or nanodiscs, in the absence or presence of BL. Each point represents means ± SD, calculated from three technical replicates within this experiment ($n = 3$). (**B**) ATPase activities of ABCB19 in DDM-CHS or nanodiscs in the presence of increasing concentrations of BL. Each point represents means ± SD, calculated from three technical replicates within this experiment ($n = 3$). (**C**) Topological representation of the ABCB19. The TM helices 1 to 6 and NBD1 are colored light blue, and the TM helices 7 to 12 and NBD2 are in light orange. The R domain is indicated with a red dashed box. (**D**) Side view of the cryo-EM map of substrate-free ABCB19 in nanodiscs. (**E**) Side view of the substrate-free ABCB19 in ribbon representation. All domains are colored as in (C).

Substrate binding induces inward movement of ABCB19

The substantially higher activity of ABCB19 in nanodiscs compared to that in detergents strongly argues that lipid membrane is essential for characterizing the function and structure of ABCB19. Furthermore, substrate stimulation of ATPase activity of several ABC transporters is associated with conformational transition upon substrate binding (*9*, *23*, *25*). However, a previous study of ABCB19 in detergents did not observe structural difference after adding BL (*11*). To reveal the potential impact of BL binding on ABCB19 conformation, we set out to determine and compare the structures of nanodisc-embedded ABCB19 in the absence or presence of BL.

The cryo-EM map of the substrate-free ABCB19 at 4.1-Å resolution revealed an inward-facing conformation with the NBDs well separated (figs. S5 and S9A). Typical of type IV ABC transporters, the transmembrane (TM) helices are arranged in a domain-swapped manner, with transmembrane domain (TMD) 1 formed by TMs 1, 2, 3, 10, 11, and 6 and TMD2 formed by TMs 7, 8, 9, 4, 5, and 12. Notably, a flexible break region in TM10 (K856-A866) divides the helix into two parts, TM10a and TM10b (Fig. 1, C to E). This flexible region is at the level of the inner membrane leaflet and likely facilitates substrate entry from the membrane. Within the cavity between the two TMDs, an extra density was clearly resolved with the size and shape consistent with a lipid molecule (fig. S2, A to D). It is conceivable that this lipid stabilizes the inward-facing conformation of ABCB19 and is subsequently replaced by substrates with high affinity to the inner cavity. When compared to the previously reported ABCB19 substrate-free structure in detergent [Protein Data Bank (PDB): 8woi], the structure in the nanodisc exhibits a larger opening facing the cytoplasmic side, leading to an overall root mean square deviation (RMSD) of 3.341 Å, and the distance at the bottom of the nucleotide-binding domain (NBD) has increased by 9.6 Å (fig. S10, A and B), likely expanding the available space for substrate entry. Distinct from previously reported ABCB19 structure in detergents, the linker between NBD1 and TMD2, so-called R domain, was not observed in our cryo-EM map, likely due to conformational flexibility (Fig. 1, C to E). Considering the hypothesis that the R domain is involved in ABCB19 inhibition (*11*), the lack of stable R domain in our structure is in line with the robust activity of membrane-embedded ABCB19, and ABCB19 in detergents with stabilized R domain is likely in an inhibited state.

To generate the structure of BL-bound ABCB19, nanodisc-embedded ABCB19 was incubated with 50 μM BL and subjected to single-particle cryo-EM analysis (fig. S6). The resulting cryo-EM

map at 3.6-Å resolution demonstrated clear side-chain densities in the TMDs and enabled accurate model building (Fig. 2, A and B, and figs. S2, E to H, and S9B). Compared to substrate-free ABCB19, BL-bound ABCB19 clearly showed that TM helices shifted toward the center (Fig. 2, C and D). Such shifts gradually increased from the distal ends of the TMDs to the NBDs, resulting in a decrease in the distance between the NBDs by more than 8 Å. The more open conformation in substrate-free structure suggests a primed state ready for substrate recognition and entry. The substrate binding-induced inward movement has been observed in other type IV ABC transporters, such as ABCC1 (*31*), ATM3 (*9*), and TmrAB (*32*, *33*).

Compared to the previous BL-bound ABCB19 structure in detergents, the TMDs and BL interacting amino acids are essentially identical, and more observable differences are in the NBDs leading to an overall RMSD of 2.167 Å (over 1166 Cα atoms) (fig. S10, C and D). BL formed hydrophobic interactions with residues F58, F59, and F62 in TM1, Y276 in TM5, F309 in TM6, as well as F953, V954, V957, and I958 in TM12. Hydrogen bonding with W283 suggests that a relatively defined interaction network is required for substrate binding and stabilization within the cavity (Fig. 2D), as previously reported (*11*). Structure superimposition of BL-bound ABCB19 and ABCB1 (PDB: 8WOM, 8ZPZ, and 9JUL) shows that the binding modes of BL are highly conserved in ABCB19 and ABCB1 (fig. S11A). To better understand the importance of the BL-interacting amino acids, they were each mutated and tested for basal and BL-stimulated ATPase activities. These mutations demonstrated varied effects on the basal activity of ABCB19, with four (F58Q, F59Q, Y276A, and V957Q) showing little changes ("basal-wt"), five (F62Q, W283Q, F309Q, F953Q, and V954Q) stimulated by 1.7- to 2.5-fold ("basal-high"), and one (I958Q) inhibited by 41% ("basal-low") (Fig. 2E and fig. S4). Among the "basal-wt" mutations, F58Q and F59Q led to substantial decrease in BL stimulation, and the effect of Y276A was moderate, together indicating that these three residues play important roles in BL binding; in contrast, V957Q did not affect BL binding. Despite decreased basal activity, I958Q showed robust BL stimulation, showing lack of effect on BL binding. For the "basal-high" mutations, it is less straightforward to derive their impacts on BL interaction. Nevertheless, the activities of F62Q, F309Q, and F953Q were still much lower than that of BL-stimulated wild-type ABCB19, and unchanged upon BL addition, suggesting that these two mutations affect BL binding. In sum, our results show that F58, F59, F62, Y276, F309, and F953 are critical amino acids for BL binding. (Fig. 2E).

Stabilization of nucleotide-bound ABCB19 is temperature dependent

During the functional cycles of ABC transporters, ATP binding-induced NBD dimerization causes structural rearrangement of TMDs. To stabilize such a conformation for biochemical and structural studies, researchers often incubate ABC transporters with ATP analogs, such as ADP-vanadate (*23*, *24*), ATPγS (*34*), and AMPPNP (*35*), or use catalytically deficient mutants that bind but not hydrolyze ATP (*15*, *16*, *36*). For type IV ABC transporters, these procedures effectively convert the nucleotide-free, often inward-open, conformations to the nucleotide-bound, often closed or outward-open, conformations. Therefore, a previous report is puzzling that, like nucleotide-free ABCB19, wild-type ABCB19 with AMPPNP and catalytically deficient mutant with ATP display an inward-open conformation (*11*).

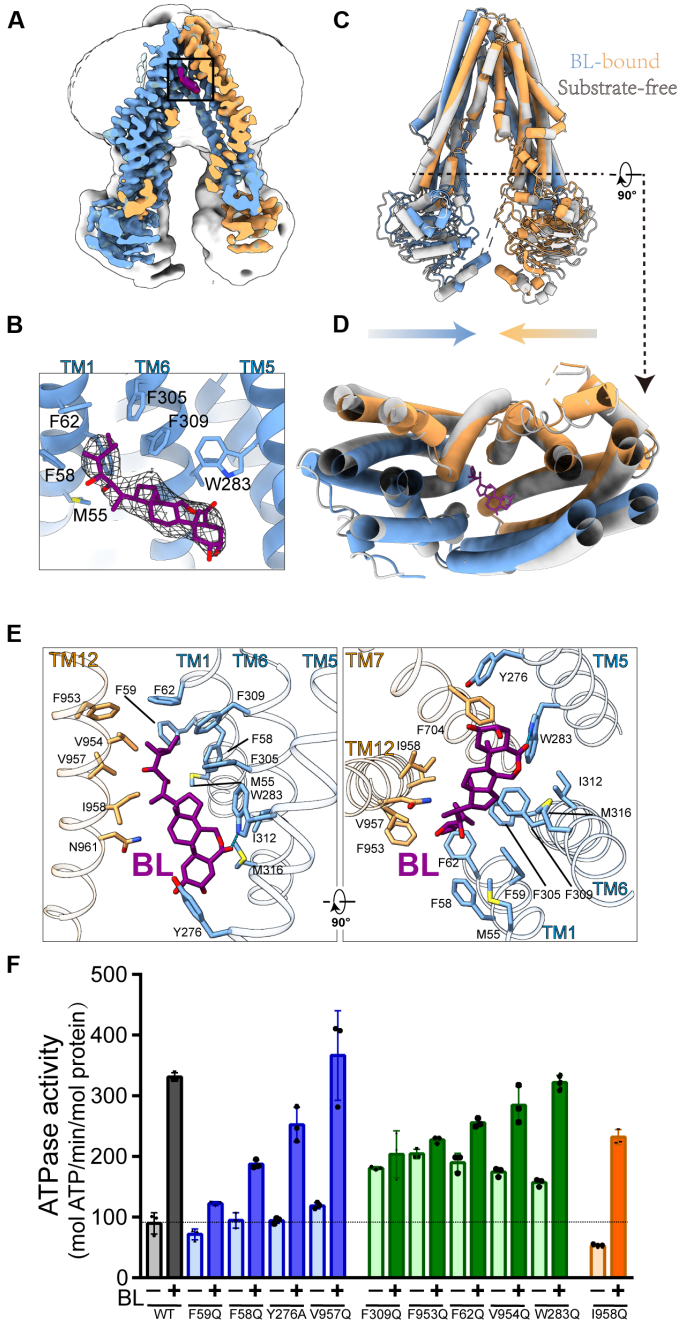

Fig. 2. BL binding to ABCB19. (**A**) Side view of the cryo-EM map of BL-bound ABCB19 in nanodiscs. BL is colored purple. All protein domains are colored as in Fig. 1C. (**B**) Zoomed-in view of BL [box in (A)], showing the EM density (black mesh) superimposed with the atomic model. (**C**) Superimposition of the BL-bound (light blue and orange) and substrate-free (gray) ABCB19 structures, shown in the same view as in (A). (**D**). Bottom-up view from the level shown in (C) (black dashed line). (**E**) Side and bottom-up views of the BL binding site, with the BL in purple and the interacting amino acids in light blue and orange. (**F**) ATPase activities of wild-type and mutant ABCB19 in the absence or presence of 2 μM BL. Each point represents means ± SD, calculated from three technical replicates within this experiment ($n = 3$). The dashed line indicates the activity of wild-type ABCB19 without BL.

Our own initial attempts of trapping ABCB19 with vanadate also demonstrated a predominantly inward-open conformation characterized by well-separated NBDs (fig. S3, A and B). A scrutiny of experimental details revealed that all these assays incubated ABCB19 proteins with nucleotides on ice. Such a low temperature differs from 37°C, which is used in ATPase assays (Fig. 3A), and possibly hinders the conformational transition of ABCB19. The ATPase activity of ABCB19 on ice is much lower than that at 37°C (fig. S1G). After vanadate trapping was performed at 37°C, as shown in cryo-EM two-dimensional (2D) and 3D classification, most proteins were stabilized in the close conformation characterized by tightly dimerized NBDs (fig. S3, C and D). Considering that nucleotide-bound conformations can be stabilized at a low temperature for many other type IV ABC transporters including Pgp (*37*), MsbA (*23*), and PCAT1 (*38*), the more strict temperature dependence of ABCB19 is intriguing and warrants future studies.

The cryo-EM structure of vanadate-trapped ABCB19 was determined at 3.7-Å resolution, showing a closed conformation with the inner cavity completely collapsed (Fig. 3B and figs. S8 and S9D). This represents a functional state after substrate release and before returning to the inward-open conformation. Compared to the substrate-free state, vanadate-trapped ABCB19 displayed large-scale conformational changes in both NBDs and TMDs. The two NBDs tightly dimerized, with the ADP-vanadate complexes bound at both ATP-binding sites. The Walker A and signature motifs coordinated the ADP-vanadate complex along with Mg^{2+}, and the well-defined cryo-EM densities of ATP-binding sites showed nearly identical contacts between the ADP-vanadate complex and surrounding residues. Specifically, Y1019 can form a π-π interaction with the aromatic ring of ATP, and R1022 further stabilizes the binding of ATP (Fig. 3, C and D). The ATP binding site on the opposite side exhibits a similar binding mode. The reorganization of the TMDs is characterized by the inward movements of TMs 6 and 12 to collapse the inner cavity, as well as the closure of TMs 4 and 5 and TMs 10 and 11 to bring the NBDs together (Fig. 3E). TM10, which is interrupted by a flexible region in the inward-facing conformation, transforms into a continuous helix after vanadate trapping, sealing the intracellular gate and preventing substrate backflow or leakage (Fig. 3F). Structure superimposition of closed ABCB19 and outward-facing ABCB1 (PDB: 9JUP) shows that their overall conformations are highly similar. However, ABCB1 exhibits a distinct outward bending particularly at the top of TM1 and TM2, which is not observed in ABCB19 (fig. S11B). Such bending and slight TMD opening at the distal end of the TMDs may facilitate substrate release.

Inhibitor BUM occupies substrate pocket and blocks conformational transition

The development of small-molecule inhibitors targeting ABCB transporters is driven by its pivotal role in regulating hormone transport, a fundamental process influencing plant morphogenesis (*39*, *40*). 2-[4-(Diethylamino)-2-hydroxybenzoyl]benzoic acid (BUM) has been identified as a specific ABCB inhibitor, exhibiting a markedly lower median inhibitory concentration (IC_{50}) value compared to traditional inhibitors and making it a more potent ABCB inhibitor (*17*). However, the mechanism of plant ABCB inhibitors is poorly understood, which hinders the rational development of specific and effective plant growth regulators.

BUM demonstrated a concentration-dependent inhibition of ABCB19, with an IC_{50} value of 0.89 mM (Fig. 4A). BUM may stop ABCB19 by blocking its conformational changes or slow down the transport cycle by functioning as a difficult substrate. To better

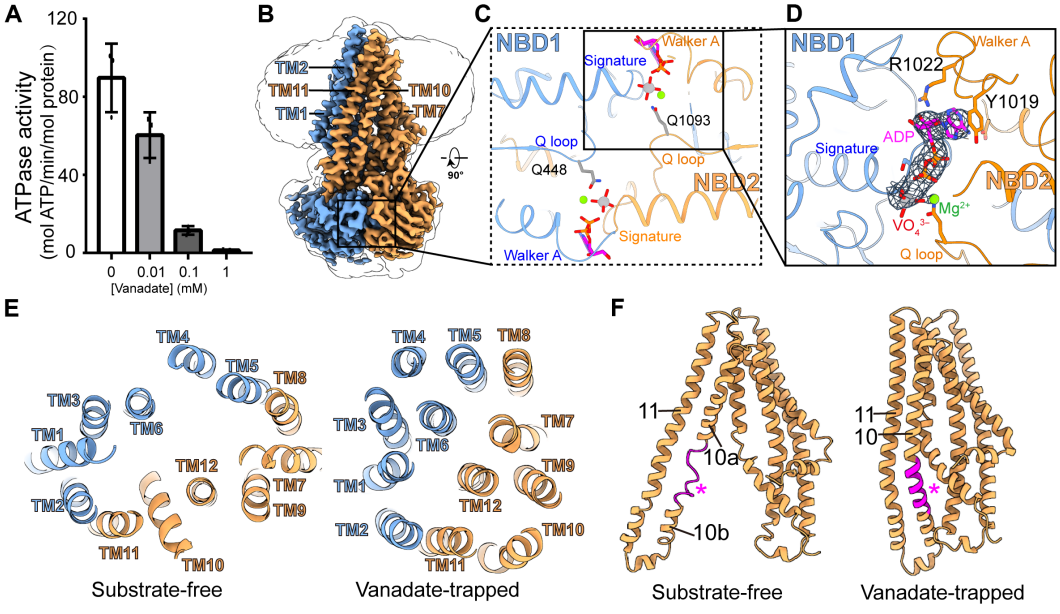

Fig. 3. Closed conformation of vanadate-trapped ABCB19. (**A**) ATPase activity of nanodisc-embedded ABCB19 in the presence of increasing concentrations of vanadate. Each point represents means ± SD, calculated from three technical replicates within this experiment ($n = 3$). (**B**) Side view of the cryo-EM map of vanadate-trapped ABCB19. All protein domains are colored as in Fig. 1C. (**C**) Zoomed-in view of the ATP binding sites [box in (B)]. (**D**) Zoomed-in view of the structure of an ADP-vanadate-Mg^{2+} complex [box in (C)] superimposed with the EM density (black mesh). (**E**) Cross-sectional views of the TM helices of substrate-free and vanadate-trapped ABCB19. (**F**) Side views of the TM helices 7 to 12 in the substrate-free and vanadate-trapped ABCB19, with the flexible region within TM10 colored in magenta and indicated by a star.

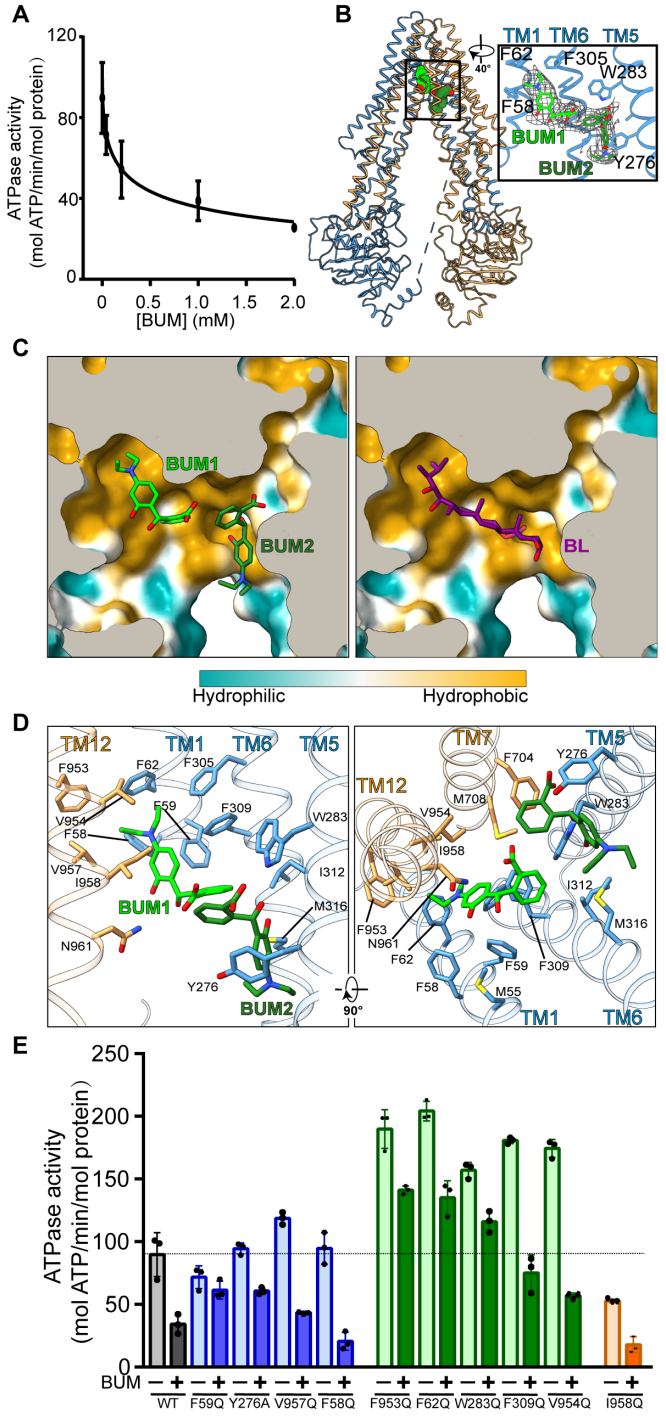

Fig. 4. BUM binding to ABCB19. (**A**) ATPase activities of nanodisc-embedded ABCB19 in the presence of increasing concentrations of BUM. Each point represents means ± SD, calculated from three technical replicates within this experiment ($n = 3$). (**B**) Side view of the structure of BUM-bound ABCB19, with a zoomed-in view of the two bound BUM molecules superimposed with the EM density (gray mesh). (**C**) Cross-sectional views of BUM and BL binding in ABCB19, with the protein shown in hydrophobicity surface and BUM (green) and BL (purple) in sticks. (**D**) Side and bottom-up views of the BUM binding site. (**E**) ATPase activities of wild-type and mutant ABCB19 in the absence or presence of 1 mM BUM. Each point represents means ± SD, calculated from three technical replicates within this experiment ($n = 3$). The dashed line indicates the activity of wild-type ABCB19 without BUM.

understand the inhibition mechanism, we compared the conformational changes induced by vanadate incubation in the presence and absence of BUM. The presence of 1 mM BUM caused ABCB19 to remain in the inward-open form with separated NBDs (fig. S3E), whereas in the absence of BUM, most ABCB19 proteins were converted to the closed form with tightly dimerized NBDs. (fig. S3, C and D). These results indicate that BUM exerts its inhibitory effect by locking ABCB19 in the inward-open conformation.

To understand the structural basis of BUM inhibition, ABCB19 with 1 mM BUM was subjected to single-particle cryo-EM analysis (fig. S7). The resulting cryo-EM structure at 3.8-Å resolution demonstrates an inward-open conformation (Fig. 4B and figs. S2, I to L, and S9C). Compared to the substrate-free state, the BUM-bound ABCB19 displays a clear inward movement with an RMSD of 3.047 Å (over 1166 Cα atoms) (fig. S10, E and F). Both with inward movements compared to the substrate-free ABCB19, the BUM- and BL-bound structures display nearly identical TMDs and similar NBDs (RMSD of 2.529 Å over 1166 Cα atoms) (fig. S10, G and H). Two distinct densities were resolved between the TMDs, and each density fits one BUM (termed BUM1 and BUM2) (Fig. 4B). These two BUM molecules together occupy a hydrophobic pocket, which overlaps closely with the BL binding pocket (Fig. 4C). When displayed at a high contour level, the part of BUM2 near BUM1 became slightly weaker whereas the distal part of BUM2 remained strong (fig. S2, I to L). These observations indicate that both BUM molecules are bound to ABCB19 rather tightly, and there seems no strong interaction between BUM1 and BUM2. The occupation of substrate-binding pocket by two molecules of inhibitor has been reported for other type IV ABC transporters such as the Pgp inhibitor zosuquidar (*41*) and the MsbA inhibitor TBT1 (*42*).

When superimposed, the diethylamino group of BUM1 overlaps with the methyl groups of BL, protruding into a hydrophobic pocket formed by M55, F58, F59, and F62 in TM1, F305, and F309 in TM6, and F953, V957, I958, and N961 in TM12. BUM1 and BL adopt a similar orientation, but because the BUM molecule is smaller than BL, the ring moieties of BL extend to the position occupied by BUM2, interact with Y276 and W283 in TM5 (Fig. 4D). Among the "basal-wt" mutations, F59Q led to substantial decrease in BUM inhibition, and the effect of Y276A was moderate, together indicating that these two residues play important roles in BUM binding; in contrast, F58Q and V957Q did not affect BUM binding. Despite decreased basal activity, I958Q showed robust BUM inhibition, showing lack of effect on BUM binding. For the "basal-high" mutations, the activities of F62Q, W283Q, and F953Q were altered slightly upon BUM addition and remained substantially higher than that of BUM-inhibited wild-type ABCB19, suggesting that these mutations affect BUM binding as well. In sum, F59, F62, Y276, W283, and F953 are the critical amino acids for BUM binding (Fig. 4E). Together with the findings from mutagenesis studies on BL stimulation, F59, F62, Y276, and F953 are involved in the binding of both substrate and inhibitor, F58 and F309 are specifically associated with BL interaction, and W283 are exclusively associated with BUM binding (table S2).

DISCUSSION

Reconstitution of ABCB19 into nanodiscs markedly enhanced ATPase activity compared to detergents, indicating that nanodiscs better mimics the native membrane environment to support transporter function. Our study revealed the distinct conformations

of nanodisc-embedded ABCB19 in its substrate-free, BL (substrate)–bound, vanadate-trapped, and BUM (inhibitor)–bound states, delineating the key conformational steps in the transporter cycle and uncovering the mechanism of inhibitor. On the basis of our results and knowledge in the field, we propose a working model of ABCB19 transport cycle (Fig. 5). First, ABCB19 adopts an inward-open conformation in the substrate-free state. A flexible break in the middle of TM10 likely facilitates substrate entry. Second, substrate binding to the inner pocket induces an inward movement of the TMDs and NBDs, and binding of the inhibitor BUM induces similar conformational changes. Third, upon ATP binding, dimerization of the NBDs leads to an outward-facing conformation of ABCB19, promoting substrate efflux. However, the inhibitor BUM occupying the substrate binding pocket blocks conformational transition and renders the transporter nonfunctional. Fourth, after substrate release, ABCB19 transforms into a fully closed conformation. The subsequent ATP hydrolysis and release allow ABCB19 to return to the initial inward-open conformation.

Compared to detergent-solubilized protein, nanodisc-embedded ABCB19 demonstrated a lower concentration of BL for activation, and a concentration-dependent effect on ATPase activity, where low BL concentrations enhanced, and high concentrations inhibited activity. The comparison of substrate-free and BL-bound structures demonstrated a BL-induced closure of ABCB19, suggesting that the more open conformation is more favorable for substrate entry. The substrate entry, in turn, closes the transporter to bring NBDs closer to facilitate the ATP binding and subsequent conformational changes.

We discovered an unexpected temperature dependence of forming stable nucleotide-bound conformation of ABCB19. In the presence of vanadate, 37°C, but not lower temperatures, resulted in a fully closed conformation. This distinct temperature sensitivity may be related to the unique physiological roles of plant ABCB proteins, potentially enhancing the plant's ability to cope with temperature stress by regulating hormone transport. The mechanism underlying different temperatures required for ABC transporters to stabilize the conformation with tightly dimerized NBDs needs further investigation.

Our study elucidated the structural basis of ABCB19 inhibitor BUM, an ABCB-specific inhibitor that restricts plant growth, particularly root elongation (*17*). Two BUM molecules interact within the substrate pocket, which is reminiscent of the inhibitors for other type IV ABC transporters, suggesting a common mode of inhibition for these transporters with similar folds. The positioning of the two BUM molecules also suggests a route for the substrates to enter from the lower part of the inner cavity. BUM and the BL substrate overlapped closely within the hydrophobic pocket between TMDs. Mutagenesis experiments reveal that certain residues in the pocket (F58, F309, and V954) are specifically associated with the binding of BL but not BUM. Particularly, the F309Q mutation resulted in increased basal activity compared to the wild type but markedly reduced BL-induced activation, highlighting the role of F309 in establishing the hydrophobic substrate-binding pocket and facilitating substrate binding. The structural and mechanistic understanding of ABCB19 function and inhibition will accelerate rational development of small molecules and facilitate the creation of safer and more effective plant growth regulators.

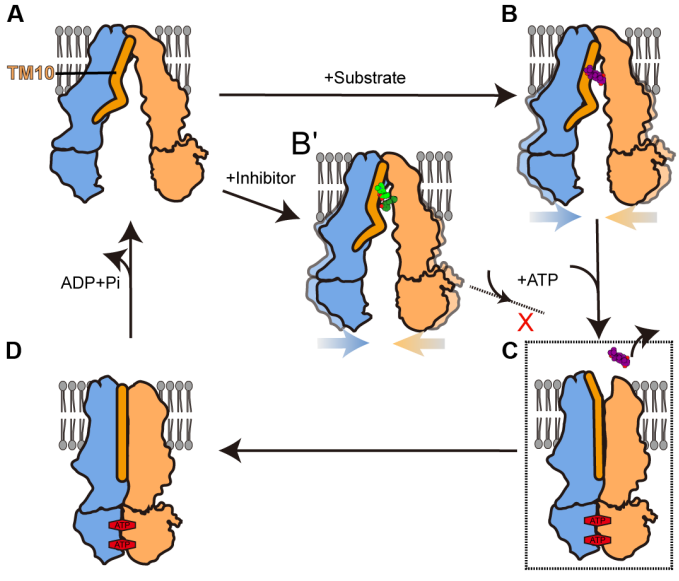

Fig. 5. Working model for the transport cycle of ABCB19. All protein domains are colored as in Fig. 1C. The TM10 kinking indicates the flexible region within TM10. Substrate, inhibitor, and ATP are colored purple, green, and red, respectively. The key functional states include (**A**) inward-facing substrate-free, (**B**) inward-facing to bind substrate, (**B′**) inward-facing to bind inhibitor, (**C**) outward-facing with bound ATP to expel substrate, and (**D**) closed after substrate release. See text for description of the proposed transport cycle of ABCB19.

MATERIALS AND METHODS

Construction of protein expression plasmids

The gene of *Arabidopsis* ABCB19 was codon optimized and synthetized by GeneScript (Piscataway, NJ). For protein production, the ABCB19 sequence was cloned into the pSBtet vector with a C-terminal GFP-strepII sequence and a Tobacco Etch Virus (TEV) protease cleavage site between them. The gene of *Arabidopsis* TWD1 was amplified from the *Arabidopsis* complementary DNA library and cloned into the psBbi vector. All the mutants were produced by the Quickchange Site-Directed Mutagenesis Kit (New England Biolabs, Ipswich, MA), and all the plasmids were sequenced for verification.

Expression and purification of ABCB19

Expression and purification of ABCB19 were modified based on a previously described procedure (*43*). ABCB19 from *Arabidopsis* was expressed in HEK293 freestyle cells (Thermo Fisher Scientific, Waltham, MA), using a transposon-based inducible stable cell line system (*44*). First, the TWD1 stable cell line was generated by cotransfection of the pSBbi-TWD1 and SB-100X transponse vector, followed by a week of G418 selection. The ABCB19 stable cell line was generated by cotransfection of the pSBtet-ABCB19 and the SB-100X transpose vector into TWD1 stable cell line, followed by a week of puromycin selection. The cells were grown in suspension at 37°C in FreeStyle 293 Expression Medium (Union, Shanghai, China). When the cells reached a density of 4×10^6 cells/ml, doxycycline (2 μg/ml) and 2 mM sodium butyrate were added to the cells to induce the protein production and boost the expression, respectively. The temperature was set to 30°C. The cultures were harvested after 48 hours. The cells were washed once in ice-cold phosphate-buffered saline and then flash frozen in liquid nitrogen and stored in −80°C or placed on ice for immediate use.

All protein purification steps were performed at 4°C. Thawed cell pellets were resuspended in the lysis buffer containing 50 mM tris-HCl (pH 7.5), 300 mM NaCl, 10% glycerol, 5 mM $MgCl_2$, and DNase

I and supplemented with 1× complete protease inhibitor cocktail. DDM/CHS detergent (final concentration of 1%/0.2%) (Anatrace, Maumee, OH) was added to lyse the cells for 2 hours. Insoluble debris was removed by centrifugation 150,000*g* for 60 min, and the supernatant was incubated with Strep-Tactin Sepharose beads (IBA, Göttingen, Germany) for 3 hours. The resin was then washed with ~100 ml of washing buffer (lysis buffer containing 0.1%DDM/0.02%CHS).

For protein purification in detergents, the protein were eluted using elution buffer (wash buffer containing 50 mM biotin), and then TEV proteases were added into the eluted proteins to remove the GFP and strep tag before the elution was concentrated by a 100-kDa MWCO spin concentrator and injected onto a Superose 6 column (GE Healthcare, Chicago, IL) equilibrated with 25 mM tris-HCl (pH 7.5), 150 mM NaCl, and 0.05%DDM/0.01%CHS. The peak fractions containing ABCB19 were pooled and concentrated to ~5 mg/ml.

On-column nanodisc reconstitution

Following procedures previously described in (*45*), with modifications, MSP1D1 and POPG were premixed at a molecular ratio of 1:70, and this mixture was incubated with ABCB19-bound strep resin at a 3:1 (v/v) ratio, followed by gentle agitation 1 hour in the cold room. Detergent was then removed by incubation with Bio-Beads SM-2 (Bio-Rad, Hercules, CA) overnight. The resin was then washed with ~100 ml of nanodisc buffer [25 mM tris-HCl (pH 7.8) and 150 mM NaCl] and eluted using nanodisc elution buffer (nanodisc buffer containing 50 mM biotin), and then TEV protease were added to the eluted nanodisc-reconstituted ABCB19 to remove the GFP and strep tag before the eluted protein was concentrated by a 100-kDa MWCO spin concentrator and injected onto a Superdex 200 increase 10/300 GL column equilibrated with nanodisc buffer. The peak fractions containing nanodisc-embedded ABCB19 were pooled and concentrated to ~2 mg/ml.

ATPase assay

All ATPase activity assays, including inhibition by vanadate or BUM, and stimulation by substrate, were modified from a previously described procedure (*24*). Forty micrograms of purified ABCB19 in detergent or 4 μg of ABCB19 in lipid nanodiscs was prewarmed with reaction solution containing 50 mM Hepes (pH 7.5), 100 mM NaCl, and 4 mM $MgCl_2$ for 5 min at 37°C, ATP was added to the solution at a final concentration of 2 mM, and the reaction was initiated in a final volume of 25 μl at 37°C for 20 min. The reaction was stopped by adding 25 μl 12% (w/v) SDS. Fifty microliters of solution containing equal volumes of 12% (w/v) ascorbic acid in 1 M HCl and 2% (w/v) ammonium molybdate in 1 M HCl was added and incubated for 5 min at room temperature. Addition of 75-μl solution containing 25 mM sodium citrate, 2% (w/v) sodium metarsenite, and 2% (v/v) acetic acid was followed by incubation for 20 min at room temperature. Absorbance at 850 nm was measured using the SpectraMax iD3 (Molecular Devices, San Jose, CA), and potassium phosphate in a concentration range from 0.05 to 0.8 mM was used as a standard for determining the concentration of released phosphate. Vanadate inhibition assays were carried out in the presence of sodium orthovanadate.

For the substrate-stimulated or BUM-inhibited ATPase activity assay, substrate or BUM was diluted to 100 times desired final concentration with dimethyl sulfoxide, added to the wild-type or mutant protein-containing mixture, and incubated on ice for 30 min, followed by prewarming and initiating the reaction at 37°C for 20 min in a final volume of 25 μl.

EM sample preparation and data collection

EM sample preparation and data collection were modified based on previously described procedures (*23*, *26*). Negatively stained specimens were prepared following an established protocol (*46*) with minor modifications. Specifically, 4 μl of purified ABCB19 in detergents or nanodiscs were applied to glow-discharged copper EM grids covered with a thin layer of continuous carbon film, and the grids were stained with 2% (w/v) uranyl acetate (EMCN, Beijing, China). These grids were imaged on a Talos L120C electron microscope (Thermo Fisher Scientific) operated at 120 kV at a nominal magnification of 92,000× using a 4k × 4k charge-coupled device camera (Thermo Fisher Scientific), corresponding to a calibrated pixel size of 1.52 Å on the specimen level.

For cryo-EM, 3.5 μl of purified nanodisc-embedded ABCB19 at a concentration of 2 mg ml^{-1} were applied to a freshly glow-discharged Quantifoil holey carbon grid (1.2/1.3, 400 mesh) (Quantifiol, Jena, Germany). Grids were blotted for 3.5 s with ~100% humidity and plunge frozen in liquid ethane using Vitrobot (Thermo Fisher Scientific). For the preparation of cryo-EM samples of BL or BUM-bound ABCB19, 0.05 mM BL or 1 mM BUM were added into the nanodisc-embedded ABCB19 sample and incubated on ice for 30 min. For vanadate trapped sample, 2 mM ATP, 4 mM $MgCl_2$, and 1 mM sodium orthovanadate were added into the nanodisc-embedded ABCB19 sample and incubated at 37°C for 10 min.

Cryo-EM data were collected at liquid nitrogen temperature on a Tatan Krios transmission electron microscope (Thermo Fisher Scientific), operated at 300 kV and equipped with Falcon4 (Thermo Fisher Scientific) or K3 direct electron detector (Gatan). The movies of substrate-free ABCB19 were recorded using Falcon4 with a pixel size of 1.074 Å. The dose rate was set to be 7.46 electrons per physical pixel per second. The total exposure time of each movie was 7.74 s, leading to a total accumulated dose of 50 electrons/$Å^2$, fractionated into 32 frames. The movies of ADP vanadate-bound, BL-bound, or BUM-bound ABCB19 were recorded in super-resolution counting mode using K3 with a calibrated pixel size of 0.855 Å on the specimen level and 0.428 Å for super-resolution images. The dose rate was set to be 25 electrons per physical pixel per second. The total exposure time of each movie was 1.46 s, leading to a total accumulated dose of 50 electrons/$Å^2$, fractionated into 32 frames. All movies were recorded with a defocus ranging from 1.0 to 2.0 μm. The detailed data collection parameters are listed in table S1.

EM data processing

Negative-stain EM images were initially selected using SamViewer and a semiautomated procedure implemented in Simplified Application Managing Utilities for EM Labs (SAMUEL) (*47*). 2D classification was performed with "samclasscas.py," "samtree2dv3.py," or 2D classification in RELION-3.0 (*48*).

For cryo-EM data, motion correction and dose weighting were performed using the EMshark implementation of MotionCor2 (*49*).

Substrate-free and BL-bound datasets were imported into cryoSPARC to determine their defocus values and contrast transfer function (CTF) parameters using Patch CTF Estimation (*50*). Particles were picked by blob picker or template picker and were then extracted for 2D classification. Junk particles were removed by several rounds of 2D classification. The initial 3D model was generated using ab initio reconstruction. Junk particles were also removed by heterogeneous refinement. The best classes were used for nonuniform refinement to enhance the resolution. Nonuniform refinement was

carried out with *C*1 symmetry. The overall resolution of each map was determined using the gold-standard Fourier shell correlation (FSC) = 0.143 criterion. Local resolution estimation for each map was generated using cryoSPARC.

For BUM and vanadate dataset, defocus values were calculated using CTFFIND4 (*51*). 2D classification of selected particle images was carried out by "sambatch2d.py," which uses SPIDER operations to run 10 cycles of correspondence analysis, *K*-means classification, and multireference alignment. Initial 3D models were generated with 2D class averages by SPIDER 3D projection matching refinement (samrefine.py), starting from a cylindrical density mimicking the general shape and size of nanodisc-embedded ABCB19. 3D classification and refinement were carried out in RELION-5.0. Detailed image processing parameters related to cryo-EM image processing are summarized in table S1.

Model building and refinement

The initial model of ABCB19 was generated using AlphaFold2 or AlphaFold3 and docked into the cryo-EM maps using UCSF Chimera (*52*, *53*). Manual model building and adjustment were then performed using Coot (*54*). The structures were refined by real-space refinement using PHENIX (*55*). Because our vanadate-trapped ABCB19 adopts a closed conformation, we used AlphaFold3 to generate a model of vanadate-trapped ABCB19 by inputting the protein sequence along with two ATP molecules and two Mg^{2+} ions. ABCB19 and fitted it into the cryo-EM map, and the model was improved by several rounds of manual adjustment in Coot and refinement using phenix.real_space_refine. All structure figures were prepared in PyMOL (https://pymol.org/2/), UCSF Chimera, and ChimeraX (*56*).

Supplementary Materials

This PDF file includes:

Figs. S1 to S11

Tables S1 and S2

REFERENCES AND NOTES

1. A. M. Plummer, A. T. Culbertson, M. Liao, The ABCs of sterol transport. *Annu. Rev. Physiol.* **83**, 153–181 (2021).
2. C. F. Higgins, Multiple molecular mechanisms for multidrug resistance transporters. *Nature* **446**, 749–757 (2007).
3. D. C. Rees, E. Johnson, O. Lewinson, ABC transporters: The power to change. *Nat. Rev. Mol. Cell Biol.* **10**, 218–227 (2009).
4. K. P. Locher, Mechanistic diversity in ATP-binding cassette (ABC) transporters. *Nat. Struct. Mol. Biol.* **23**, 487–493 (2016).
5. A. L. Davidson, E. Dassa, C. Orelle, J. Chen, Structure, function, and evolution of bacterial ATP-binding cassette systems. *Microbiol. Mol. Biol. Rev.* **72**, 317–364 (2008).
6. T. H. T. Do, E. Martinoia, Y. Lee, Functions of ABC transporters in plant growth and development. *Curr. Opin. Plant Biol.* **41**, 32–38 (2018).
7. J. Kang, J. Park, H. Choi, B. Burla, T. Kretzschmar, Y. Lee, E. Martinoia, Plant ABC transporters. *Arabidopsis Book* **9**, e0153 (2011).
8. J. U. Hwang, W. Y. Song, D. Hong, D. Ko, Y. Yamaoka, S. Jang, S. Yim, E. Lee, D. Khare, K. Kim, M. Palmgren, H. S. Yoon, E. Martinoia, Y. Lee, Plant ABC transporters enable many unique aspects of a terrestrial plant's lifestyle. *Mol. Plant* **9**, 338–355 (2016).
9. C. Fan, D. C. Rees, Glutathione binding to the plant AtAtm3 transporter and implications for the conformational coupling of ABC transporters. *Elife* **11**, (2022).
10. H. Wei, H. Zhu, W. Ying, H. Janssens, M. Kvasnica, J. M. Winne, Y. Gao, J. Friml, Q. Ma, S. Tan, X. Liu, E. Russinova, L. Sun, Structural insights into brassinosteroid export mediated by the *Arabidopsis* ABC transporter ABCB1. *Plant Commun.* **6**, 101181 (2025).
11. W. Ying, Y. Wang, H. Wei, Y. Luo, Q. Ma, H. Zhu, H. Janssens, N. Vukasinovic, M. Kvasnica, J. M. Winne, Y. Gao, S. Tan, J. Friml, X. Liu, E. Russinova, L. Sun, Structure and function of the *Arabidopsis* ABC transporter ABCB19 in brassinosteroid export. *Science* **383**, eadj4591 (2024).
12. Q. Chen, L. Zhu, S. Zhang, S. Qiao, Z. J. Ding, S. J. Zheng, J. Guo, N. Su, Structures and mechanisms of the ABC transporter ABCB1 from *Arabidopsis thaliana*. *Structure* **33**, 903–915.e5 (2025).
13. N. An, X. Huang, Z. Yang, M. Zhang, M. Ma, F. Yu, L. Jing, B. Du, Y. F. Wang, X. Zhang, P. Zhang, Cryo-EM structure and molecular mechanism of the jasmonic acid transporter ABCG16. *Nat. Plants* **10**, 2052–2061 (2024).
14. X. Huang, X. Zhang, N. An, M. Zhang, M. Ma, Y. Yang, L. Jing, Y. Wang, Z. Chen, P. Zhang, Cryo-EM structure and molecular mechanism of abscisic acid transporter ABCG25. *Nat. Plants* **9**, 1709–1719 (2023).
15. W. Ying, L. Liao, H. Wei, Y. Gao, X. Liu, L. Sun, Structural basis for abscisic acid efflux mediated by ABCG25 in *Arabidopsis thaliana*. *Nat. Plants* **9**, 1697–1708 (2023).
16. J. Xin, Y. Zhou, Y. Qiu, H. Geng, Y. Wang, Y. Song, J. Liang, K. Yan, Structural insights into AtABCG25, an angiosperm-specific abscisic acid exporter. *Plant Commun.* **5**, 100776 (2024).
17. J. Y. Kim, S. Henrichs, A. Bailly, V. Vincenzetti, V. Sovero, S. Mancuso, S. Pollmann, D. Kim, M. Geisler, H. G. Nam, Identification of an ABCB/P-glycoprotein-specific inhibitor of auxin transport by chemical genomics. *J. Biol. Chem.* **285**, 23309–23317 (2010).
18. M. Geisler, A. S. Murphy, The ABC of auxin transport: The role of p-glycoproteins in plant development. *FEBS Lett.* **580**, 1094–1102 (2006).
19. N. L. Mellor, U. Voss, A. Ware, G. Janes, D. Barrack, A. Bishopp, M. J. Bennett, M. Geisler, D. M. Wells, L. R. Band, Systems approaches reveal that ABCB and PIN proteins mediate co-dependent auxin efflux. *Plant Cell* **34**, 2309–2327 (2022).
20. J. Mravec, M. Kubes, A. Bielach, V. Gaykova, J. Petrasek, P. Skupa, S. Chand, E. Benkova, E. Zazimalova, J. Friml, Interaction of PIN and PGP transport mechanisms in auxin distribution-dependent development. *Development* **135**, 3345–3354 (2008).
21. H. S. Robert, J. Friml, Auxin and other signals on the move in plants. *Nat. Chem. Biol.* **5**, 325–332 (2009).
22. M. Cho, H. T. Cho, The function of ABCB transporters in auxin transport. *Plant Signal. Behav.* **8**, e22990 (2013).
23. W. Mi, Y. Li, S. H. Yoon, R. K. Ernst, T. Walz, M. Liao, Structural basis of MsbA-mediated lipopolysaccharide transport. *Nature* **549**, 233–237 (2017).
24. Y. Li, B. J. Orlando, M. Liao, Structural basis of lipopolysaccharide extraction by the $LptB_2FGC$ complex. *Nature* **567**, 486–490 (2019).
25. B. J. Orlando, M. Liao, ABCG2 transports anticancer drugs via a closed-to-open switch. *Nat. Commun.* **11**, 2264 (2020).
26. S. Sharma, R. Zhou, L. Wan, S. Feng, K. Song, C. Xu, Y. Li, M. Liao, Mechanism of LolCDE as a molecular extruder of bacterial triacylated lipoproteins. *Nat. Commun.* **12**, 4687 (2021).
27. B. Wang, A. Bailly, M. Zwiewka, S. Henrichs, E. Azzarello, S. Mancuso, M. Maeshima, J. Friml, A. Schulz, M. Geisler, *Arabidopsis* TWISTED DWARF1 functionally interacts with auxin exporter ABCB1 on the root plasma membrane. *Plant Cell* **25**, 202–214 (2013).
28. M. K. Jenness, R. Tayengwa, G. A. Bate, W. Tapken, Y. Zhang, C. Pang, A. S. Murphy, Loss of multiple ABCB auxin transporters recapitulates the major twisted dwarf 1 phenotypes in *Arabidopsis thaliana*. *Front. Plant Sci.* **13**, 840260 (2022).
29. Z. Wei, J. Li, Brassinosteroids regulate root growth, development, and symbiosis. *Mol. Plant* **9**, 86–100 (2016).
30. R. W. Robey, S. Shukla, E. M. Finley, R. K. Oldham, D. Barnett, S. V. Ambudkar, T. Fojo, S. E. Bates, Inhibition of P-glycoprotein (ABCB1)- and multidrug resistance-associated protein 1 (ABCC1)-mediated transport by the orally administered inhibitor, CBT-1 ((R)). *Biochem. Pharmacol.* **75**, 1302–1312 (2008).
31. Z. L. Johnson, J. Chen, Structural basis of substrate recognition by the multidrug resistance protein MRP1. *Cell* **168**, 1075–1085.e9 (2017).
32. C. Thomas, R. Tampe, Structural and mechanistic principles of ABC transporters. *Annu. Rev. Biochem.* **89**, 605–636 (2020).
33. S. Hofmann, D. Januliene, A. R. Mehdipour, C. Thomas, E. Stefan, S. Bruchert, B. T. Kuhn, E. R. Geertsma, G. Hummer, R. Tampe, A. Moeller, Conformation space of a heterodimeric ABC exporter under turnover conditions. *Nature* **571**, 580–583 (2019).
34. C. A. J. Hutter, M. H. Timachi, L. M. Hurlimann, I. Zimmermann, P. Egloff, H. Goddeke, S. Kucher, S. Stefanic, M. Karttunen, L. V. Schafer, E. Bordignon, M. A. Seeger, The extracellular gate shapes the energy profile of an ABC exporter. *Nat. Commun.* **10**, 2260 (2019).
35. A. Ward, C. L. Reyes, J. Yu, C. B. Roth, G. Chang, Flexibility in the ABC transporter MsbA: Alternating access with a twist. *Proc. Natl. Acad. Sci. U.S.A.* **104**, 19005–19010 (2007).
36. L. T. M. Le, J. R. Thompson, S. Dehghani-Ghahnaviyeh, S. Pant, P. X. Dang, J. B. French, T. Kanikeyo, E. Tajkhorshid, A. Alam, Cryo-EM structures of human ABCA7 provide insights into its phospholipid translocation mechanisms. *EMBO J.* **42**, e111065 (2023).
37. Y. Kim, J. Chen, Molecular structure of human P-glycoprotein in the ATP-bound, outward-facing conformation. *Science* **359**, 915–919 (2018).
38. V. Kieuvongngam, J. Chen, Structures of the peptidase-containing ABC transporter PCAT1 under equilibrium and nonequilibrium conditions. *Proc. Natl. Acad. Sci. U.S.A.* **119**, (2022).

39. M. K. Jenness, R. Tayengwa, A. S. Murphy, An ATP-binding cassette transporter, ABCB19, regulates leaf position and morphology during phototropin1-mediated blue light responses. *Plant Physiol.* **184**, 1601–1612 (2020).
40. K. Okamoto, H. Ueda, T. Shimada, K. Tamura, Y. Koumoto, M. Tasaka, M. T. Morita, I. Hara-Nishimura, An ABC transporter B family protein, ABCB19, is required for cytoplasmic streaming and gravitropism of the inflorescence stems. *Plant Signal. Behav.* **11**, e1010947 (2016).
41. A. Alam, J. Kowal, E. Broude, I. Roninson, K. P. Locher, Structural insight into substrate and inhibitor discrimination by human P-glycoprotein. *Science* **363**, 753–756 (2019).
42. F. A. Thelot, W. Zhang, K. Song, C. Xu, J. Huang, M. Liao, Distinct allosteric mechanisms of first-generation MsbA inhibitors. *Science* **374**, 580–585 (2021).
43. S. Wang, K. Wang, K. Song, Z. W. Lai, P. Li, D. Li, Y. Sun, Y. Mei, C. Xu, M. Liao, Structures of the *Mycobacterium tuberculosis* efflux pump EfpA reveal the mechanisms of transport and inhibition. *Nat. Commun.* **15**, 7710 (2024).
44. E. Kowarz, D. Loscher, R. Marschalek, Optimized Sleeping Beauty transposons rapidly generate stable transgenic cell lines. *Biotechnol. J.* **10**, 647–653 (2015).
45. A. M. Plummer-Medeiros, A. T. Culbertson, C. L. Morales-Perez, M. Liao, Activity and structural dynamics of human ABCA1 in a lipid membrane. *J. Mol. Biol.* **435**, 168038 (2023).
46. D. S. Booth, A. Avila-Sakar, Y. Cheng, Visualizing proteins and macromolecular complexes by negative stain EM: From grid preparation to image acquisition. *J. Vis. Exp.* **58**, 3227 (2011).
47. H. Ru, M. G. Chambers, T. M. Fu, A. B. Tong, M. Liao, H. Wu, Molecular mechanism of V(D)J recombination from synaptic RAG1-RAG2 complex structures. *Cell* **163**, 1138–1152 (2015).
48. S. H. Scheres, RELION: Implementation of a Bayesian approach to cryo-EM structure determination. *J. Struct. Biol.* **180**, 519–530 (2012).
49. S. Q. Zheng, E. Palovcak, J. P. Armache, K. A. Verba, Y. Cheng, D. A. Agard, MotionCor2: Anisotropic correction of beam-induced motion for improved cryo-electron microscopy. *Nat. Methods* **14**, 331–332 (2017).
50. A. Punjani, J. L. Rubinstein, D. J. Fleet, M. A. Brubaker, cryoSPARC: Algorithms for rapid unsupervised cryo-EM structure determination. *Nat. Methods* **14**, 290–296 (2017).
51. A. Rohou, N. Grigorieff, CTFFIND4: Fast and accurate defocus estimation from electron micrographs. *J. Struct. Biol.* **192**, 216–221 (2015).
52. J. Jumper, R. Evans, A. Pritzel, T. Green, M. Figurnov, O. Ronneberger, K. Tunyasuvunakool, R. Bates, A. Zidek, A. Potapenko, A. Bridgland, C. Meyer, S. A. A. Kohl, A. J. Ballard, A. Cowie, B. Romera-Paredes, S. Nikolov, R. Jain, J. Adler, T. Back, S. Petersen, D. Reiman, E. Clancy, M. Zielinski, M. Steinegger, M. Pacholska, T. Berghammer, S. Bodenstein, D. Silver, O. Vinyals, A. W. Senior, K. Kavukcuoglu, P. Kohli, D. Hassabis, Highly accurate protein structure prediction with AlphaFold. *Nature* **596**, 583–589 (2021).
53. E. F. Pettersen, T. D. Goddard, C. C. Huang, G. S. Couch, D. M. Greenblatt, E. C. Meng, T. E. Ferrin, UCSF Chimera—A visualization system for exploratory research and analysis. *J. Comput. Chem.* **25**, 1605–1612 (2004).
54. P. Emsley, B. Lohkamp, W. G. Scott, K. Cowtan, Features and development of Coot. *Acta Crystallogr. D Biol. Crystallogr.* **66**, 486–501 (2010).
55. P. D. Adams, P. V. Afonine, G. Bunkoczi, V. B. Chen, I. W. Davis, N. Echols, J. J. Headd, L. W. Hung, G. J. Kapral, R. W. Grosse-Kunstleve, A. J. McCoy, N. W. Moriarty, R. Oeffner, R. J. Read, D. C. Richardson, J. S. Richardson, T. C. Terwilliger, P. H. Zwart, PHENIX: A comprehensive Python-based system for macromolecular structure solution. *Acta Crystallogr. D Biol. Crystallogr.* **66**, 213–221 (2010).
56. E. F. Pettersen, T. D. Goddard, C. C. Huang, E. C. Meng, G. S. Couch, T. I. Croll, J. H. Morris, T. E. Ferrin, UCSF ChimeraX: Structure visualization for researchers, educators, and developers. *Protein Sci.* **30**, 70–82 (2021).

Acknowledgments: We thank the assistance of Southern University of Science and Technology (SUSTech) Cryo-EM Center. M.L. is an investigator of SUSTech Institute for Biological Electron Microscopy. **Funding:** This work was supported by the Guangdong Innovative and Entrepreneurial Research Team Program 2023ZT10Y013 and Shenzhen Medical Research Fund B2302043. **Author contributions:** M.L. supervised the project. Y.L. designed and performed experiments. Y.L. and M.L. analyzed the data. M.L. and Y.L. wrote the manuscript. **Competing interests:** The authors declare that they have no competing interests. **Data and materials availability:** Model coordinates and cryo-EM density maps for the ABCB19 structures in substrate-free, BL-bound, BUM-bound, and ADP vanadate-trapped states have been deposited in the Protein Data Bank with accession codes 9KG2, 9KJC, 9KKE, and 9KK6, respectively, and in the Electron Microscopy Data Bank with accession codes EMD-62306, EMD-62366, EMD-62385, and EMD-62383, respectively. All other data needed to evaluate the conclusions in this paper are present in the paper and/or the Supplementary Materials.

Submitted 15 January 2025
Accepted 9 May 2025
Published 13 June 2025
10.1126/sciadv.adv9721